







Multidimensional nanoscopic chiroptics

Yang Chen, Wei Du , Qing Zhang, Oscar Ávalos-Ovando , Jing Wu , Qing-Hua Xu, Na Liu, Hiromi Okamoto , Alexander O. Govorov, Qihua Xiong  and Cheng-Wei Qiu 

Abstract | Nanoscopic chiroptics studies the spin-dependent asymmetric light–matter interactions at the nanoscale, where the asymmetry can stem from the intrinsic properties of materials, structures, light or combinations thereof. With the emergence of low-dimensional materials platforms, such as metasurfaces, transition metal dichalcogenides and perovskites, nanoscopic chiroptics has been extended from the far field to the near field, and further developed from the spatial dimension, to the momentum dimension and the integrated spatial–momentum dimension. This expansion of nanoscopic chiroptics across dimensions has uncovered new physical mechanisms and manifestations of chiral effects. It also led to applications such as valleytronics, chiral sensing and chiral photochemistry. This Perspective focuses on the progress in nanoscopic chiroptics through the lens of the associated dimensionalities, discussing the opportunities in integrated optics, photochemistry, quantum optics and biochemical synthesis and analysis.

Chirality, as first defined by Lord Kelvin¹, refers to the geometric symmetry property of an object that cannot be superposed onto its mirror image using rotations and translations. The modern definition of chirality, based on group theory, is: the geometric property of an object lacking symmetry elements of the second kind (a mirror plane, $\sigma=S_1$; a centre of inversion, $i=S_2$; a rotation–reflection axis, S_{2n})^{2,3}. A photon associated with a circularly polarized field also has an internal degree of freedom of spin angular momentum (SAM). Light–matter interaction, thus, has a potential to induce an exchange of angular momentum between the electronic spin of a material and circularly polarized light (CPL). As a result, chiral materials may exhibit different optical properties when interacting with CPL of different handedness^{4–6}, a field known as chiroptics. Chiroptics is particularly important in enantiomer separation⁷, disease diagnosis⁸ and drug development⁹.

In the past decades, the study of chiroptics expanded into the nanoscale regime, while its scope has evolved (see Fig. S1 in the Supplementary Information). The emergence of low-dimensional materials, including chiral perovskites¹⁰,

transition metal dichalcogenides (TMDCs)¹¹ and chiral quantum dots¹², has provided new platforms for realizing chiroptical effects. Apart from materials engineering, the structural configuration can also endow chiroptical properties to originally achiral materials. Chiral metamaterials and metasurfaces constructed by nanofabrication techniques have demonstrated extraordinary chiroptical properties that are not attainable in naturally occurring objects^{13–17}. In addition, the properties of incident light, including wavelength, polarization and incident direction, are closely related to the generation of chiroptical effects as well. Achiral nanostructures could still show chiroptical properties for CPL with in-plane linear momentum¹⁸ or orbital angular momentum (OAM)¹⁹. In this way, chiroptics is generalized as a branch of optics that studies the photon spin-dependent asymmetry in light–matter interactions, where the asymmetry can originate from the particular properties of materials, structures, light or their combinations.

Advances in nanomaterials and nanostructures, together with the progress in light science, have facilitated the rapid

growth of nanoscopic chiroptics. Now, chiral asymmetry is not only studied in the far field, through the measurement of refraction, absorption and radiative emission, but also investigated in the near field (see Fig. S1 in the Supplementary Information). When nanostructures are illuminated by light, the optical twist of the generated near field can be greater than that of free-space CPL, which promises applications in chiral sensing^{20–31}, photochemistry^{32–34} and photoemitters^{35–37}. Apart from the spatial dimension, far field and near field, the research of chiroptics has more recently been extended to the momentum dimension (see Fig. S1 in the Supplementary Information) and the integrated spatial–momentum dimension. Photons with opposite spins can have a different behaviour in the momentum space, due to spin–orbit coupling (SOC)³⁸. The development of chiroptics across these dimensions has uncovered new physical mechanisms and manifestations of chiroptical effects, which not only provide tools to investigate chiroptical phenomena but also enable applications in sensing²⁸, photochemistry^{34,39} and spintronics^{40,41}.

The near-field spatial dimension

The near field is the region of the electromagnetic (EM) field in the close vicinity of an object, typically extended for less than one wavelength. When nanomaterials are illuminated by EM waves, optical chirality is induced in the near field (BOX 1). As a related quantity, the optical chirality flux $\tilde{\mathbf{F}}$ is defined as:

$$\tilde{\mathbf{F}} = \frac{1}{2} [\tilde{\mathbf{E}} \times (\nabla \times \tilde{\mathbf{B}}) - \tilde{\mathbf{B}} \times (\nabla \times \tilde{\mathbf{E}})], \quad (1)$$

where $\tilde{\mathbf{E}}$ and $\tilde{\mathbf{B}}$ are electric and magnetic fields, respectively. The following equation of the conservation law can be derived⁴²:

$$\begin{aligned} \frac{\partial \tilde{C}}{\partial t} + \frac{1}{\mu_0} \nabla \cdot \tilde{\mathbf{F}} \\ = -\frac{1}{2} [\tilde{\mathbf{J}} \cdot \nabla \times \tilde{\mathbf{E}} + \tilde{\mathbf{E}} \cdot \nabla \times \tilde{\mathbf{J}}], \end{aligned} \quad (2)$$

where $\tilde{\mathbf{J}}$ denotes the electric current in the material, \tilde{C} denotes the optical chirality and μ_0 denotes the vacuum permeability. $\tilde{\mathbf{F}}$, $\tilde{\mathbf{J}}$, $\tilde{\mathbf{B}}$, $\tilde{\mathbf{E}}$ and \tilde{C} are all time-dependent quantities. If $\tilde{\mathbf{J}} = 0$, the summation of the

Box 1 | Origin of chiroptical effects

Within the framework of classical electromagnetism, the linear electric and magnetic polarizations, \mathbf{p} and \mathbf{m} , induced on the chiral material by the external electromagnetic field are correlated with the electric (\mathbf{E}) and the magnetic (\mathbf{B}) fields by the following constitutive equations⁴²:

$$\mathbf{p} = \alpha\mathbf{E} - iG\mathbf{B}, \quad (3)$$

$$\mathbf{m} = \chi\mathbf{B} + iG\mathbf{E}. \quad (4)$$

α , χ and G are frequency-dependent complex scalars, $\alpha = \alpha' + i\alpha''$, $\chi = \chi' + i\chi''$ and $G = G' + iG''$. They denote the electric, magnetic and mixed electric-magnetic polarizability, respectively. The ordinary absorption and refraction of light by matter arise mainly from the first term of Eq. (3), whose oscillation phase shift does not depend on the handedness of incident CPL. However, due to the phase difference between the \mathbf{B} and \mathbf{E} fields of the CPL, the contribution of the second term in Eq. (3) and the second term in Eq. (4) is opposite for the right-handed and left-handed circularly polarized (RCP and LCP, respectively) light. Thus, a non-zero G parameter is the origin of chiroptical effects. The local absorption of RCP (+) and LCP (−) light $A(\mathbf{r})^\pm$ by chiral materials is expressed as⁴²:

$$A(\mathbf{r})^\pm = \frac{\omega}{2}(\alpha'' |\mathbf{E}|^2 + \chi'' |\mathbf{B}|^2) \mp \frac{2}{\epsilon_0} G'' C, \quad (5)$$

where C denotes the optical chirality, a quantity relevant to the twist of the local electromagnetic field, and μ_0 is the free-space magnetic permeability. C is expressed as⁴²:

$$C(\mathbf{r}) = -\frac{1}{2}\omega\epsilon_0\text{Im}[\mathbf{E}^* \cdot \mathbf{B}], \quad (6)$$

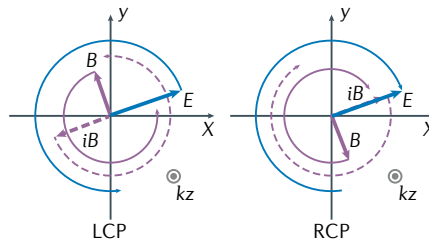
For the free-space light with fixed frequency (ω) and intensity, the absolute value of C becomes maximum for the pure CPL, while the sign of C is opposite for RCP and LCP light. The position-dependent analogue of circular dichroism is differential absorption (DA), defined as⁴²:

$$DA(\mathbf{r}) = \frac{4}{\epsilon_0} G'' C(\mathbf{r}), \quad (7)$$

According to Eq. (7), a strong twist of the local field, as indicated by a large $|C(\mathbf{r})|$, is the key factor for enhancing near-field chiral effects.

temporal change of \tilde{C} and the outflow of $\tilde{\mathbf{F}}$, as represented by the first and second terms on the left side of Eq. (2), respectively, is conserved. To break the conservation of optical chirality, an electric current flowing in the material ($\tilde{\mathbf{J}} \neq 0$) is necessary^{13–45}, and the right side of Eq. (2) represents the change (creation or dissipation) of the optical chirality. It follows that, when nanomaterials resonantly interact with light in the near-field regime, the optical chirality of incident light changes due to the electronic excitation of the material (which generates $\tilde{\mathbf{J}}$), which results in the change (enhancement or suppression) of the optical chirality (FIG. 1a). For plasmonic materials, a surface plasmon current, originating from the collective oscillation of free electrons, is generated. For dielectric materials, a displacement current is instead created.

Superchiral field. Due to the scale mismatch between the wavelength of free-space CPL and the molecular wavefunction, it is difficult for molecules to ‘sense’ the chirality of light efficiently, and, thus, the chiral light–matter interaction is usually weak¹⁶.



This situation is different in the near-field regime of plasmonic, or high-index dielectric nanostructures, where the local phase velocity and group velocity of light are slowed and a localized enhanced electric field is generated⁴⁷. The helical pitch of a circularly polarized electric field, which is given by the local wavelength of the EM field, therefore, becomes narrower than that of free-space CPL, resulting in a stronger twist of the local field. Consequently, the local optical chirality C is enhanced and the enhancement is usually quantified by normalizing to the C value of illuminated CPL. Such an EM field with a strong twist is called a superchiral EM field (referred to as superchiral field for brevity^{16,17,42}), which has great potential in applications such as chiral sensing^{20–31}, chiral light sources^{35–37} and photodetectors⁴⁸.

A superchiral field is generally created in the vicinity of chiral plasmonic nanostructures^{35,49–52}, where the C field is determined by both the incident light polarization and the handedness of the structure. Usually, C values with opposite signs are simultaneously produced in different areas (FIG. 1a). As a typical example, FIG. 1b shows

the normalized C distributions of chiral plasmonic ‘shuriken’ nanostructures⁵¹. Although superchiral fields with positive and negative signs are simultaneously generated, superchiral fields are dominantly positive (negative) for the right-handed (left-handed) nanostructure upon the illumination of right-handed circularly polarized (RCP) (left-handed circularly polarized, LCP) light. Otherwise, if the handedness of light mismatches that of the nanostructure, superchiral fields with opposite signs are created with similar intensities, resulting in a relatively weak overall chirality of the nanostructure.

Although chiral plasmonic nanostructures are widely used for superchiral field generation, the achievable C value is still limited, because the induced magnetic resonance is either weak or spectrally separated from the electric resonance. Ohmic loss is another limiting factor. According to Eq. (6) in BOX 1, the optimal platform for creating an enhanced superchiral field should possess both electric and magnetic modes, the two modes should be strong, spectrally and spatially overlapped, and parallel, with a $\pi/2$ phase difference (FIG. 1c). These conditions can be fulfilled by well-designed dielectric nanostructures^{21,23–27,31}.

The concept of bound state in the continuum (BIC) has been introduced to enhance superchiral fields^{22,29,30}. In optics, BIC refers to an EM state completely decoupled from radiation, even though they lie inside the continuum spectrum of radiating modes of the structure⁵³. It can be considered as a resonance state with no leakage and an infinite quality factor $Q = \omega_0/2\gamma$, where ω_0 and γ represent the frequency and leakage rate of the resonance, respectively. By introducing geometric perturbations, BICs become quasibound in the continuum, which are referred to as quasi-BICs⁵⁴. The quasi-BIC can couple to the radiation with high Q and, thus, boost electric and magnetic near fields significantly. Examples of nanodisc structures used for generating and enhancing superchiral fields are given in REF.²².

Near-field chiral effects. The chirality of the near field will induce near-field chiral effects, such as circularly dichroic near-field distributions, chiral photochemical effects and chiral photothermal effects, that is, the generated near-field distributions, photochemical effects or photothermal effects are different for RCP and LCP incidence. The symmetry of the near

field generated around the illuminated nanostructure depends on the symmetry of the system, including both the nanostructure and the incident light^{46,55}. As revealed by second-harmonic generation (SHG) microscopy, G-shaped chiral nanostructures show spin-dependent SHG intensity patterns (FIG. 1d), which is mainly distributed around the central square for the RCP case and around the four corners for the LCP case⁵⁶. The SHG intensity patterns can indicate the near-field distributions of plasmonic modes^{56,57}. Even if the nanostructure is highly symmetric and achiral, the symmetry of the local field can still become chiral when it is illuminated with CPL. This phenomenon was first observed in REF.⁵⁸, followed by the simulations and near-field imaging experiments^{59,60}. FIGURE 1e illustrates circularly dichroic near-field distributions for the symmetric V-shaped nanoantenna imaged using cathodoluminescence microscopy. The electric field is primarily distributed on the left arm for LCP light and is switched to the right arm for RCP incidence⁵⁹.

The mirrored near-field distributions will produce identical far-field optical responses, and, thus, the selection rule of far-field chiroptical effects (that an achiral structure is not optically active) was still satisfied. In fact, an achiral nanostructure can even exhibit near-field chirality when excited with linearly polarized light. Using polarization-resolved scanning near-field optical microscopy^{61,62}, the ellipticity angle η and azimuthal angle θ of the near-field scattered radiation was measured around a gold nanorod under linearly polarized incidence⁶³. A circularly polarized optical field was locally generated at the differential absorption active site of the nanorod, where the light–matter interactions were different for LCP and RCP light (FIG. 1f). Such local differential absorption stemmed from the local structural chirality of the anisotropic geometry.

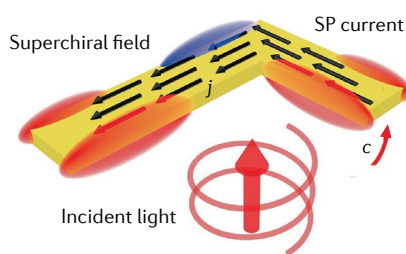
The chirality of the near field can further induce photothermal^{64–66}, photochemical^{33,34,67} and photoelectronic⁴⁸ effects, to be different for RCP and LCP incidence. These indirect chiroptical effects

are potentially useful for nanoheaters, asymmetric photocatalysis and crystal growth. However, they also provide effective methods to detect the chirality of optical near fields^{65,67}.

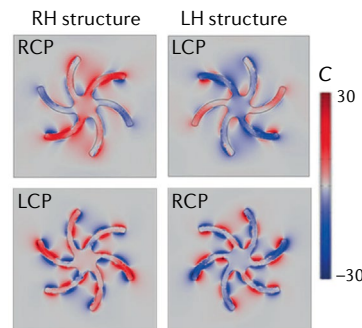
The far-field spatial dimension

The far field is the EM field region far away ($\gg \lambda$) from the object. Far-field chiroptical properties typically include circular dichroism (CD)⁶⁸, optical rotation dispersion (ORD)⁶⁹, asymmetric transmission⁷⁰ and the circular Bragg phenomenon⁷¹. The circular Bragg phenomenon refers to the almost total reflection of the CPL with a certain handedness but very little reflection of the CPL with the opposite handedness, which usually appears in cholesteric liquid crystals and chiral sculptured thin films whose chirality scales are comparable with the light wavelength⁷¹. However, this topic lies outside the scope of this Perspective. CD and ORD as measured in the far field are the collective effects of the near-field chiral properties over the entire nanostructure. Thus, although the condition for realizing near-field chirality is

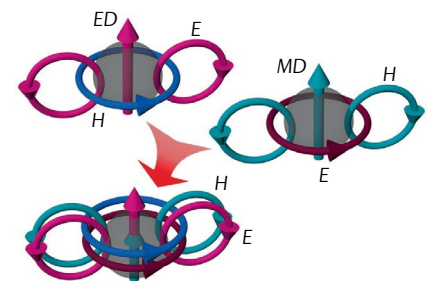
a Plasmonic superchiral field



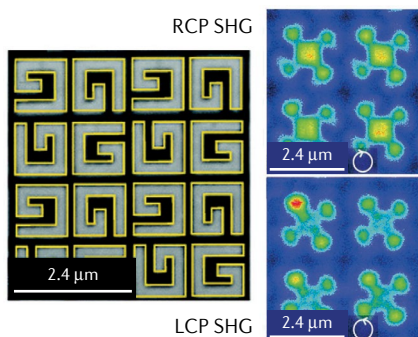
b Plasmonic nanoshuriken



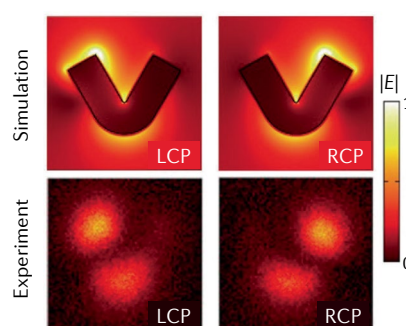
c Dielectric superchiral field



d SHG microscopy images



e Circularly dichroic E-field



f Polarization states of the near field

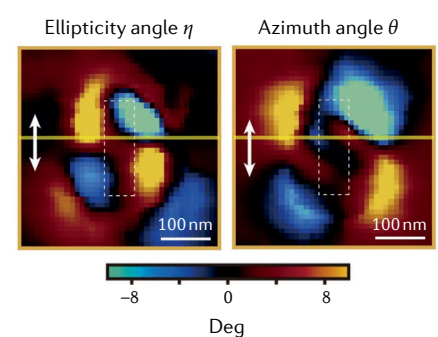
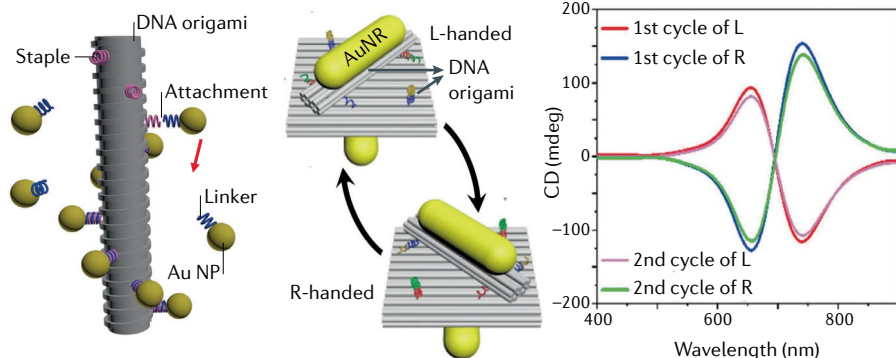


Fig. 1 | Near-field chirality. **a** | Superchiral field generated around a plasmonic nanostructure. **b** | Superchiral field distributions of the chiral plasmonic shuriken nanostructures for right-handed circularly polarized (RCP) and left-handed circularly polarized (LCP) incidence. **c** | Overlapping the electric and magnetic dual dipoles (ED and MD) of a dielectric nanostructure for the enhancement of optical chirality. **d** | Second-harmonic generation (SHG) intensity distributions of a G-shaped nanostructure array (shown on the left) for RCP and LCP illuminations.

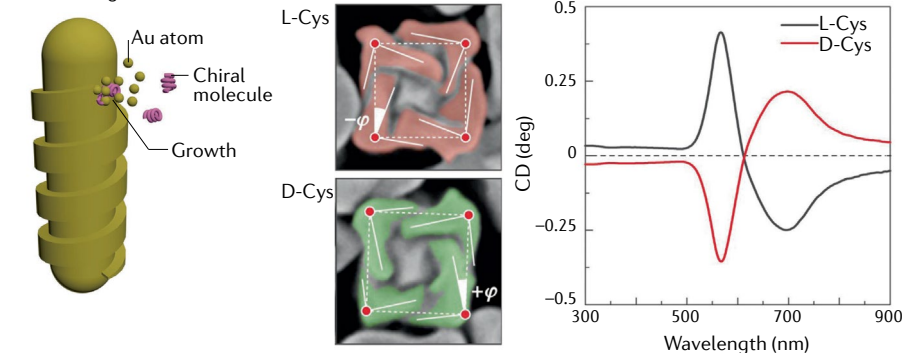
e | Circularly dichroic electric field distributions of the plasmonic V-shaped nanoantennas in simulations and experiments. **f** | Local distributions of the ellipticity angle η and azimuthal angle θ of a gold nanorod illuminated by linearly polarized light. LH, left hand; RH, right hand; SP, surface plasmon. Panel **b** adapted from REF.⁵¹, CC BY 4.0; panel **c** adapted with permission from REF.²³, ACS; panel **d** adapted with permission from REF.⁵⁶, ACS; panel **e** adapted with permission from REF.⁵⁹, ACS; panel **f** adapted with permission from REF.⁶³, ACS.

Self-assembly chiral nanomaterials

a Scaffold-based method

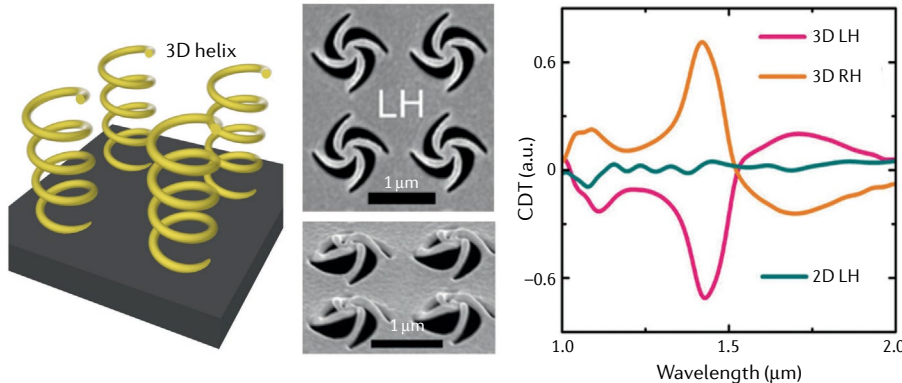


b Seeded-growth method

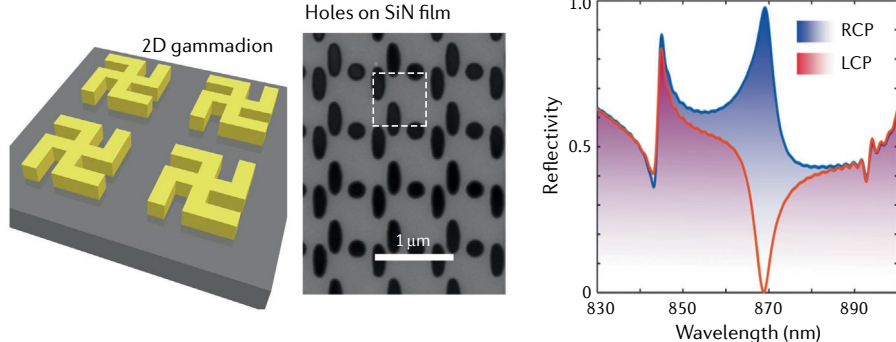


Chiral meta-optics

c Chiral metamaterials



d Chiral metasurfaces



relatively relaxed, achiral materials should be spatially structured into a handed fashion without any mirror symmetry or inversion symmetry in order to achieve chiroptical properties in the far field. Otherwise, the

contributions from different areas will cancel each other. Since many molecules intrinsically have chiral morphologies, it is natural to construct chiral nanosystems using self-assembly techniques based on these

Fig. 2 | Chiral nanosystems with far-field chiroptical properties.

Schematic illustrations of the different types of chiral nanosystems exhibiting chiroptical properties in the far field. **a** | Schematic of the scaffold-based method (left). Chiral crossed gold nanorod (AuNR) dimers assembled by DNA origami (middle). Structural reconfiguration between the left-handed and right-handed states leads to the mirrored circular dichroism (CD) spectra (right). **b** | Schematic of the seeded-growth method (left). The scanning electron microscope (SEM) images (middle) and measured CD spectra (right) of the chiral plasmonic nanocrystals as synthesized by L-Cys and D-Cys. **c** | Schematic of chiral metamaterials (left). Measured CD spectra in transmission (CDT) for 2D left-handed (LH), 3D LH and 3D right-handed (RH) pinwheel nanostructures, respectively. The SEM images of the 3D LH pinwheels are shown on the left, scale bar: 1 μ m. **d** | Schematic of chiral metasurfaces (left). The SEM image and simulated reflectivity spectra of the chiral dielectric metasurface under right-handed circularly polarized (RCP) and left-handed circularly polarized (LCP) incidence. L, left; NP, nanoparticle; R, right. Panel **a** adapted with permission from REF.⁶⁸, ACS; panel **b** adapted from REF.⁸⁶, Springer Nature Ltd; panel **c** adapted with permission of AAAS from Liu, Z. et al. Nano-kirigami with giant optical chirality. *Sci. Adv.* **4**, eaat4436 (2018) (REF.¹¹³) <https://advances.sciencemag.org/content/4/7/eaat4436.short>. The Authors, some rights reserved; exclusive licensee AAAS. Distributed under a [CC BY-NC 4.0 License](https://creativecommons.org/licenses/by-nc/4.0/). panel **d** adapted from REF.¹²², [CC BY 4.0](https://creativecommons.org/licenses/by/4.0/).

chiral molecules. Modern nanofabrication techniques enable the construction of nanostructures with chiral geometries.

Self-assembly of chiral nanomaterials.

Self-assembly directed by molecules allows for the controlled preparation of chiral plasmonic nanostructures⁷², using two strategies (FIG. 2a). The first is the scaffold-based method^{73–76}, where the molecular scaffold is dressed with helically distributed ‘staples’, while plasmonic nanoparticles (NPs) are decorated with complementary ‘linker’ strands. Through the specific binding of staples and linkers, plasmonic NPs are attached to the molecular scaffold to form a group with helical arrangement. These NPs are coupled by near-field interactions and will cooperatively show different responses to LCP and RCP light. Over the past few years, a variety of molecules have been used for the chiral assembly of plasmonic NPs, such as peptides⁷³, cysteine⁷⁴, proteins⁷⁵ and human islet amyloid polypeptides⁷⁶. DNA origami, fabricated through the folding of a long, single-stranded DNA scaffold by many shorter staple strands, offers a versatile platform for constructing chiral

plasmonic nanosystems⁷⁷. Each staple strand possesses a unique sequence and position in the folded origami nanostructure. Plasmonic NPs can be arranged at the predefined addressable sites on the DNA origami with nanometre accuracy, forming chiral plasmonic nanosystems. More importantly, DNA origami allows for the dynamic reconfiguration of the formed chiral nanostructures by multiple pathways, enabling the active tuning of the chiroptical properties^{78–80}. Such tuning schemes include strand displacement reactions⁸¹, pH regulation⁸², ion concentration⁸³ and light induction⁸⁴. For example, REF.⁶⁸ structured a crossed gold nanorod (AuNR) dimer as a chiral centre, where one AuNR was fixed at the bottom of the DNA origami plate and the other was anchored on the rotary bundle arm (FIG. 2b). The arm and plate were hinged at the centre, so that the arm, along with the attached AuNR, could rotate between the left and right states, controlled by the addition of corresponding fuel strands. Mirrored CD signals were presented for the two states.

The second self-assembly strategy is the seeded growth of chiral plasmonic nanocrystals (NCs) assisted by chiral molecules (FIG. 2a). Here, the enantioselective interactions between chiral molecules and seed NCs direct the specific deposition of metal atoms onto the NC surface, promoting the morphological evolution of seed NCs into chiral NCs^{85–88}. REFERENCE⁸⁶ demonstrated the synthesis of plasmonic helicoidal NCs assisted by amino acids and peptides (FIG. 2c). The reduction of Au⁺ ions evolved the seed NCs into high-index-plane exposed NCs, with alternating *R*-facets and *S*-facets of clockwise and anticlockwise conformation. Due to the selective absorption of chiral cysteine and cysteine-based peptides, the growth rates and directions were different in the two facets. The resulting gold helicoids generated CD signals of around 0.4° at 569 nm, and the CD signal was mirrored for NCs as synthesized by L-cysteine and D-cysteine (FIG. 2c).

Apart from plasmonic nanostructures, the self-assembly strategy has also been adopted for the preparation of chiral semiconductor crystals (such as chiral perovskites⁴⁰ and chiral quantum dots⁸⁹) and chiral metal organic frameworks^{90,91}. The synthetic combination of chirality and the intrinsic properties of these materials makes possible new applications, such as chiral perovskites for high-performance chiral sources⁹² and detectors⁹³, and chiral metal organic frameworks for asymmetric catalysis⁹⁰ and enantiomer separation⁹¹. Moreover, self-assembly chiral inorganic

crystals constitute a large chiral material family, which includes HgS, Te and TbPO₄·H₂O NCs^{94–96}, selenium chiral crystals⁹⁷ and wulffingite chiral crystals⁹⁸.

Chiral meta-optics. Although the self-assembly method is suitable for low-cost, large-scale manufacturing, it is inherently limited by the available morphologies of the molecules in nature. To overcome this limitation, chiral metamaterials composed of an array of chiral light nanoscatterers have been proposed (FIG. 2a). Compared with other types of chiral materials, such as chiral molecules and cholesteric liquid crystal, chiral metamaterials can achieve strong chiroptical responses over a thickness much smaller than the light wavelength (<0.1λ in some cases), thanks to the enhanced light–matter interactions in the near field. Besides benefiting from the flexible structural design and broad material choices (metal/dielectric/semiconductor), chiral metamaterials can have a variety of chiroptical properties, such as negative refractive index⁹⁹ and ultra-sharp CD resonance^{100–102}. Despite the high flexibility in designing 3D chiral nanostructures, their fabrication is a challenging task. In the past few years, a variety of 3D fabrication methods have been explored, such as femto-second laser direct writing^{14,103}, focused ion/electron beam (FIB/FEB) induced deposition^{104–106}, greyscale FIB milling^{107,108}, aligned lithography^{109–111} and air-pressure-actuated deformation¹¹². Recently, REF.¹¹³ used the nano-kirigami approach to construct a class of 3D chiral architectures (FIG. 2d). A 2D pattern was first cut on a suspended gold film by FIB milling and then buckled into a 3D architecture through global ion beam irradiation. The buckling process can be accurately controlled by programming the ion doses. Using this method, 3D pinwheel nanostructures were fabricated to produce large CD transmission around 1.5 μm, whereas their 2D counterparts showed no CD effects (FIG. 2d). Despite the achievements in chiral metamaterials, their future applications are impeded by the lack of mature 3D lithography techniques. To overcome these limitations, chiral metasurfaces, as the 2D version of chiral metamaterials, were introduced^{13,70,114,115} (FIG. 2a). For the typical gold gammadion metasurface, the measured ORD amplitude reached a high value of 10⁴° per mm, orders of magnitude larger than those of natural chiral substances⁶⁹. Although chiral metasurfaces with a uniform thickness have been shown to exhibit strong chiroptical responses, they cannot be considered as an approximate candidate for 3D chiral in the strictest sense due to the mirror symmetry

with respect to the *x*–*y* plane. Non-planar features created during the fabrication, such as uneven thickness and rounded edges, can break such mirror symmetry¹¹⁶.

As an alternative to plasmonic materials, dielectric materials, such as Si, SiN and TiO₂, have been explored for chiral dielectric nanostructures^{117–120}, since they can avoid the problems of low energy efficiency and large photothermal heating caused by the ohmic loss of plasmonic materials. Chiral dielectric metadevices are potentially compatible with the mature integrated circuit fabrication technology, and, thus, are well suited for industrial manufacturing. Displacement currents are excited inside dielectric nanostructures, which display both electric and magnetic responses. In the dipole approximation, the strongest optical activity is achieved when the electric and magnetic dipole vectors (*p* and *m*), as projected onto the plane normal to the *k*-vector, are parallel or antiparallel, and the sign of optical activity is opposite for these two cases^{18,121}. Accordingly, REF.¹²² reported chiral dielectric metasurfaces patterned in a SiN film (FIG. 2e). The transverse-electric-like and transverse-magnetic-like Bloch modes were responsible for the generation of in-plane electric and magnetic dipole moments, respectively, and the two modes were modulated to obtain degenerate resonant wavelengths to enlarge the scalar product *p*·*m*. The simulation results showed >97% reflection at around 870 nm for RCP light and almost no reflection for LCP light, resulting in an extinction ratio *r*₊₊/*r*₋₋ up to 1,000. Here, *r*₊₊ (*r*₋₋) denotes the RCP (LCP) reflectivity for RCP (LCP) incidence. In experiments, the extinction ratio was measured to be ≥30, a high value that is hard to realize in plasmonic systems. More recently, dielectric metamaterials have been designed to sustain chiral quasi-BICs^{100–102}. This mode is completely decoupled from the circular polarization of light, while resonantly coupled to its counterpart, and, hence, features a high *q*-factor CD resonance. Currently, the design theory for chiral meta-optics has been well studied, but its industrial application is still hindered by the available fabrication techniques.

The momentum dimension

The spatial and momentum dimensions are inherently linked by the Pontryagin duality, implying that a function given in the spatial dimension *f*(*r*) and momentum dimension *φ*(*k*) can be interconverted through Fourier transformation. Maxwell's equations inherently possess fundamental spin properties, so that the SAM of

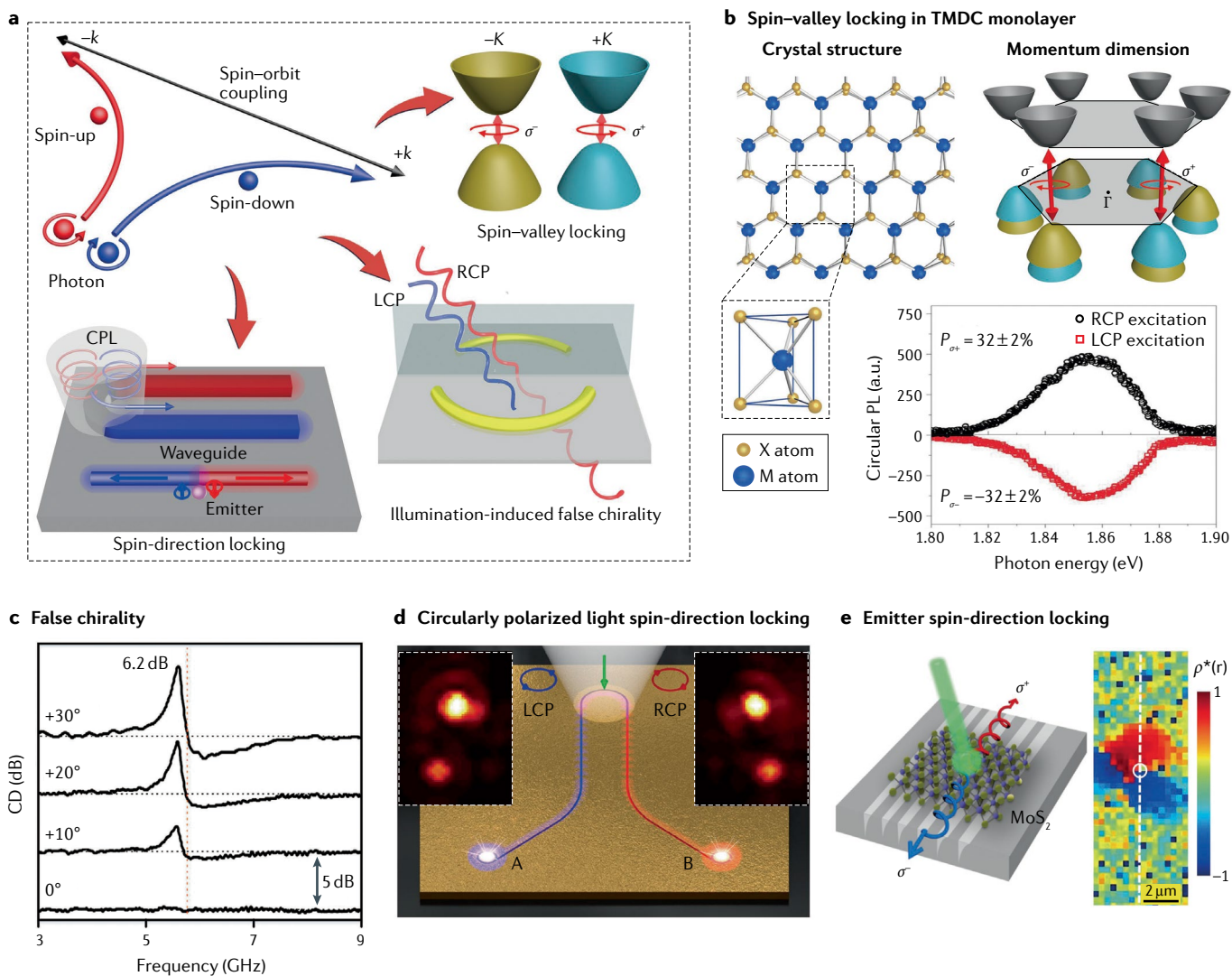


Fig. 3 | Chiral effects manifested in the momentum dimension.

a Schematic illustrations of photons with opposite spins exhibiting different behaviour in the momentum dimension through spin-orbit coupling, leading to spin-valley locking, illumination-induced false chirality and spin-direction locking. **b** Crystal and electronic structures of group VI transition metal dichalcogenide (TMDC) monolayer (MX_2). Two unequal valleys, $-K$ and $+K$, are formed in the hexagonal Brillouin zone, which are selectively coupled to σ^- and σ^+ photons for interband transitions. Representative spectra of circularly polarized photoluminescence (PL) emission for group VI TMDC monolayer are shown at the bottom. Here, the degree of valley polarization (DVP) is defined as $\text{DVP} = [I(\sigma^+) - I(\sigma^-)] / [I(\sigma^+) + I(\sigma^-)]$, where $I(\sigma^+)$ and $I(\sigma^-)$ are the helicity-resolved PL intensities

(σ^+ and σ^- stand for right-handed circularly polarized (RCP) and left-handed circularly polarized (LCP), respectively). **c** Circular dichroism (CD) spectra of the split-ring resonator measured for oblique angles α from 0° to $+30^\circ$. **d** Spin-direction locking demonstrated on an integrated optical nanocircuit for circularly polarized light incidence. The two microscopy images are obtained for LCP (left) and RCP (right) light. **e** Schematic of the valley exciton separation by coupling a MoS_2 monolayer to an asymmetric groove array (left). The measured valley polarization contrast $\rho^*(r)$ in real space is shown on the right. Panel **b** adapted from REF.¹²⁸, Springer Nature Ltd; panel **c** adapted with permission from REF.¹⁸, AIP Publishing; panel **d** adapted with permission from REF.¹⁴⁸, ACS; panel **e** adapted from REF.¹⁵⁵, Springer Nature Ltd.

light can influence its spatial degree of freedom through SOC^{38,123}. Thus, although the concept of chirality is defined in the spatial dimension, it can also manifest in the momentum dimension. Photons with opposite spins tend to undergo different trajectories in the k -space (FIG. 3a).

Spin-valley locking in group VI TMDC monolayers. Valley refers to the energetically degenerate, yet, inequivalent extrema, in the momentum space. Valley physics has

been studied in the context of information processing^{124,125}, especially with the development of 2D TMDC materials. Group VI TMDC monolayers in the form of MX_2 ($M = \text{Mo}, \text{W}; X = \text{S}, \text{Se}$) are direct bandgap semiconductors, with the band edge located at the two valleys ($+K$ and $-K$) at the corners of the hexagonal Brillouin zone (FIG. 3b). Due to the broken inversion symmetry in the unit cell, carriers in the two valleys experience opposite Berry curvature and orbital magnetic moments. Moreover, the existence

of heavy transition metal atoms yields strong SOC to lift spin degeneracy within valleys. The large spin splitting exhibits opposite signs in the two valleys¹²⁶, where only the simultaneous flip of spin and valley index is allowed during the exciton relaxation process, further contributing to the valley polarization. Such spin-valley locking is strong, enabling independent manipulation of the two valleys using CPL¹²⁷⁻¹²⁹. The interband transition at $-K$ (or $+K$) valley selectively couples to LCP (or RCP) light (FIG. 3b).

REFERENCE¹²⁸ reported a degree of valley polarization (DVP) of ~32% in the photoluminescence (PL) emission of monolayer MoS₂ at 10 K, with the helicity of PL exactly following that of the pump laser (FIG. 3b). As a reference, no valley polarization was observed in the bilayer sample for the restored inversion symmetry. Owing to the involvement of an extra energy relaxation process, the valley polarization dropped quickly with off-resonant excitation¹²⁹. Moreover, with the increase of temperature, the phonon-assisted inter-valley scattering process is accelerated, leading to the DVP in PL being rapidly decreased. This value became very weak at room temperature, which seriously hinders potential practical applications¹²⁸.

Illumination-induced false chirality.

When light is incident on a material, the illumination direction relative to the material represents an important degree of freedom. By tailoring the in-plane momentum of CPL through oblique illumination, far-field chiroptical properties can be observed for achiral materials or structures^{130–135}. This phenomenon belongs to the so-called

false chirality, which is a counterpart to true chirality. The idea of true and false chirality underlines the difference between time-invariant and non-time-invariant enantiomorphism, which was first proposed and comprehensively studied^{136–139} in the early 1980s. More recently, this phenomenon has also been realized in achiral metasurfaces illuminated by slanted CPL^{18,140–144}. For the split-ring resonator shown in FIG. 3a, optical activity is unobservable for zero transverse momentum in the *x*-direction *k_x* at normal incidence (FIG. 3c), whereas it appears and grows with increased in-plane momentum (or incidence angle)¹⁸. Apart from linear momentum, vortex beams carrying OAM can also induce chiroptical responses on an achiral platform, even under normal incidence^{19,145}. Thus, the photon momentum offers a new degree of freedom to enable chiroptical effects in achiral nanosystems.

Spin-direction locking in waveguide mode.

Another manifestation of SOC is the spin-direction locking during the excitation of waveguide mode³⁸. As depicted in FIG. 3a, chiral sources, CPL^{146–150} or chiral

emitters^{151–155} are able to produce unidirectional waveguide modes, whose direction is determined by the spin state of the source. FIGURE 3d shows the spin-direction locking of CPL realized on a plasmonic nanocircuit¹⁴⁸. The top bent waveguide served as the spin coupler for the outgoing CPL. It supported two counter-propagating gap plasmon modes carrying extrinsic OAM of $\pm\hbar\beta R$, where \hbar is the reduced Planck constant, β is the mode wavevector and *R* is the bent radius. When RCP light with SAM of $+\sigma\hbar$ was shining on the bent area, the right-propagated mode with extrinsic OAM of $+\hbar\beta R$ was excited and the out-coupled nanoantenna *B* was lightened (FIG. 3d). Instead, LCP light would lighten the nanoantenna *A*. The evanescent wave of waveguide mode plays a key role in the spin-direction locking of chiral emitters. It carries extraordinary transverse SAM, whose direction is uniquely locked with the propagation direction of the waveguide mode^{38,154}. Accordingly, REF.¹⁵⁵ coupled a MoS₂ monolayer to a subwavelength asymmetric groove array for the separation of valley excitons (FIG. 3e). Due to the asymmetric cross section of the waveguide, the $+K$ or $-K$ valley,

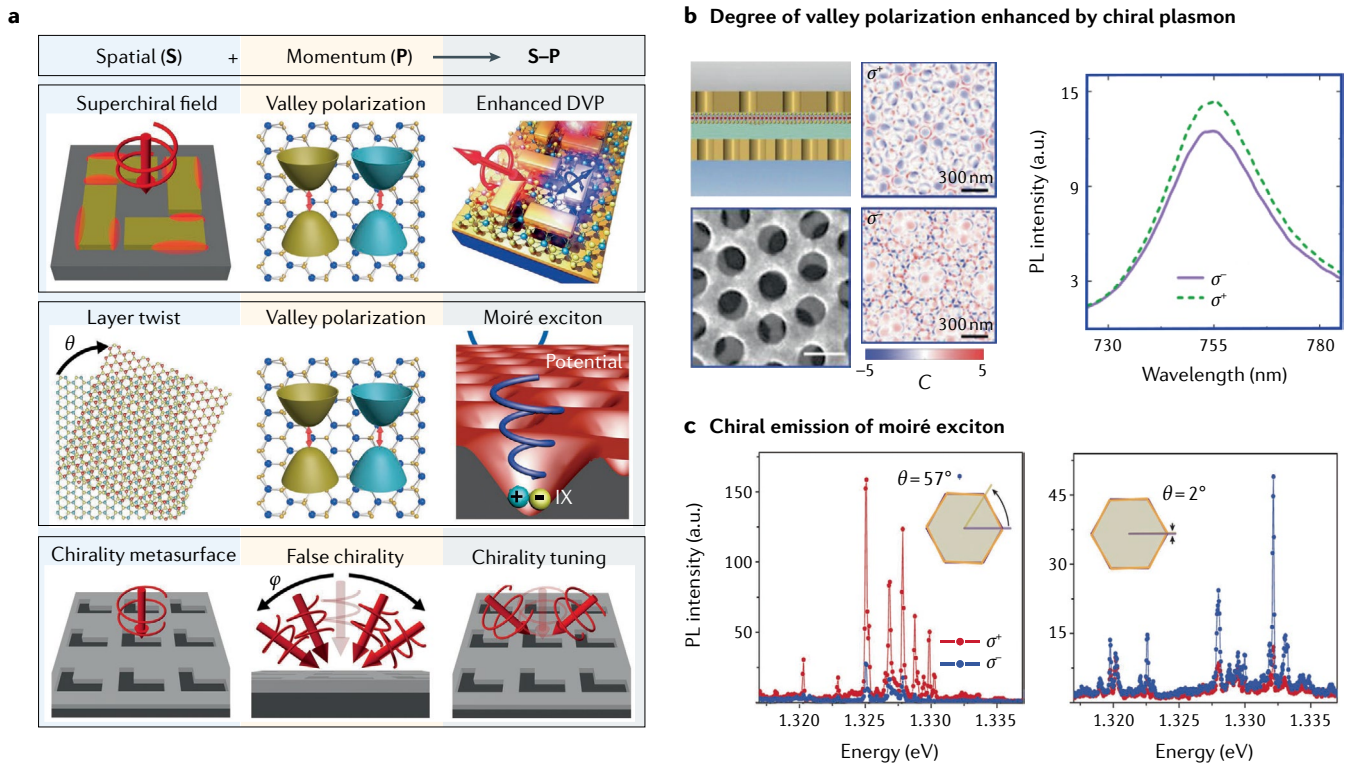


Fig. 4 | **Chiral nanosystems in the integrated spatial-momentum dimension.** **a** | Schematic illustrations of three typical examples of chiral nanosystems constructed on the integrated spatial-momentum (S-P) dimension. **b** | Hybrid nanosystem composed of a monolayer WSe₂ coupled to a chiral plasmonic metamaterial for the modulation of valley emission. Left: schematic and scanning electron microscope image of the hybrid nanosystem; middle: simulated distribution of local optical chirality *C* for the chiral

metamaterial sample ($\theta = 15^\circ$) under σ^+ and σ^- incidence at 748 nm; right: experimental helicity-resolved photoluminescence (PL) spectra of the hybrid nanosystem. **c** | Helicity-resolved PL spectra of the moiré interlayer excitons of MoX₂/WX₂ heterobilayers with twist angles of 57° and 2° under σ^+ excitation. DVP, degree of valley polarization; IX, interlayer exciton. Panel **b** adapted with permission from REF.³⁶, Wiley, 2019 WILEY-VCH Verlag GmbH & Co. KGaA, Weinheim; panel **c** adapted from REF.¹⁵⁸, Springer Nature Ltd.

acting as chiral emitters, would excite the upward-propagating or downward-propagating surface plasmon polariton guided mode, respectively. The measured spatial distribution of DVP (relative value) clearly indicated the separation of valley index. Such spin-direction locking is topologically robust and can potentially achieve nearly perfect directionality, which is a useful feature in quantum information processing.

The integrated spatial–momentum dimension

So far, we have discussed nanoscopic chiroptics in the spatial and momentum dimensions. However, the past few years have witnessed a rapid development of the chiral platforms established over the integrated spatial–momentum dimension. Chiroptical effects that cannot be realized over an individual dimension now become accessible. As mentioned above, the chiral valley emission from group VI TMDC monolayers is usually very weak at room temperature. This problem can be effectively overcome by coupling to chiral plasmonic nanostructures^{35–37} (FIG. 4a). The superchiral field generated by chiral plasmonic nanostructures will selectively modulate the excitation and spontaneous emission rates of +K and –K valley excitons. A typical example is the integrated chiral nanosystem of a WSe₂ monolayer coupled to a chiral plasmonic metamaterial³⁶ (FIG. 4b). The simulated C distributions of the chiral metamaterial are different for σ^+ and σ^- circular polarization excitation at 748 nm. Owing to the chiral Purcell effect³⁶, the spontaneous emission of +K valley became stronger than that of –K valley, leading to a stronger σ^+ PL emission and a remarkable DVP in PL at room temperature.

In addition to the strategy of combining multiple chiral components, another type of integration is realized by selecting chiral

nanomaterials from one dimension and further configuring them in the other dimension. Following this principle, two group VI TMDC monolayers with a type II band alignment are stacked and twisted into moiré heterobilayers^{156–161} (FIG. 4a). Electrons and holes will be respectively addressed in the two layers through ultra-fast charge transfer, forming interlayer excitons. Due to the twisted stacking, a periodic moiré potential is established in the superlattice, which will qualitatively change the electronic band structure of interlayer excitons. In this way, twist angle θ , as an extra degree of freedom, can strongly modulate the moiré potential landscape and, thus, influence the chiral emission of the heterostructure. REFERENCE¹⁵⁸ prepared a MoSe₂/WSe₂ moiré superlattice and measured the helicity-resolved moiré exciton PL emission (FIG. 4c). Under σ^+ excitation, the co-polarized σ^+ emission was dominant for the sample $\theta = 57^\circ$, while the cross-polarized σ^- emission was dominant for the sample $\theta = 2^\circ$.

As another example of such integration, the chiroptical band structure of a chiral metasurface was studied through oblique incidence¹⁶² (FIG. 4a). The synergic effects of the chiral geometry of a metasurface and the incident angle of CPL enable a high flexibility in chirality tuning. We believe that there will be more and more studies of the spatial–momentum-integrated chiral platforms, to meet the demand for practical applications.

Outlook

The discussed nanoscopic chiroptics effects over the near-field spatial, far-field spatial, momentum and the integrated spatial–momentum dimension and their applications are summarized in TABLE 1. This overview of the progress in nanoscopic chiroptics through the lens of the associated dimensionalities may prove useful in

the development of new directions of research. The study of chiroptics can lead to the development of optical elements, such as polarizers^{14,111}, beam generators¹⁰⁸, holograms^{108,114} and photodetectors^{93,163}. Other applications that we highlight in the Supplementary Information are found in chiral photochemistry, enantiomer separation and chiral sensing. We end by outlining some possible future directions.

Artificial intelligence has recently been introduced for the design of photonic structures^{164–166}. In sharp contrast to the traditional physics-based or rule-based approaches, it represents the data-driven methodology, which can reveal the non-intuitive relationship between the structure design and optical response. Although this topic is still in its infancy, the artificial-intelligence-based design of chiral nanostructures for realizing particular chiroptical properties could be a major trend (FIG. 5a).

Another promising direction is the use of chiral perovskite light-emitting diodes. Perovskite materials have demonstrated high external quantum efficiency for perovskite light-emitting diodes, but they usually possess weak or no intrinsic chirality. Thus, the degree of circular polarization for the emitted light is limited^{10,92} and cannot be used for those applications requiring CPL^{10,92}. One possible solution is to pattern the perovskite material into chiral geometries (FIG. 5b). The optical modes supported in the chiral nanostructures exhibit chiral asymmetry and, hence, will selectively couple to the outgoing radiation of a certain circular polarization¹⁶⁷.

Near-field chirality also has great potential for industrial applications. Currently, the study of this topic is still in the theoretical and early experimental stages, but its practical application is highly anticipated in the fields of disease diagnosis, drug development and vaccine production, especially in the context of the pandemic. For chiral sensing, dielectric metasurfaces designed by the BIC theory can generate ultra-strong superchiral fields, so that the presence of trace amounts of chiral compounds can be monitored in the CD spectrum^{22,29,30}. By further integrating the BIC metasurface onto microfluidics devices (FIG. 5c), it may lead to the portable, fast and sensitive detection devices for biological samples, such as viruses, antigens and antibodies. For enantiomer separation, the *g*-factor can be largely boosted in the near field of chiral plasmonic nanostructures, which will drive the preferential decomposition of one certain enantiomer type (FIG. 5d). Meanwhile, the low cost

Table 1 | Overview of chiroptic effects and their applications

Dimension	Effect	Applications
Far field	Circular dichroism ^{68,72,86} , optical rotation dispersion ⁶⁹ , asymmetric transmission ⁷⁰	Optical polarizer ^{14,60,111} , chiral hologram ^{108,114,117} , chiral beam generators ¹⁰⁸ , chiral light source ^{89,92} , chiral photodetector ⁹³
Near field	Superchiral field ^{23–27,42,50–52} , circularly dichroic field distributions ^{58–60} , chiral photothermal effects ^{54–56} , chiral photochemical effects ^{33,34,67} , chiral photoelectronic effects ⁴⁸	Chiral sensing ^{20–31} , chiral light source ^{35–37} , chiral photodetectors ⁴⁸ , enantiomer separation ²⁶ , chiral hot-electron generation ^{32–34}
Momentum	Spin–valley locking ^{126–129} , spin-direction locking ^{146–155} , ‘false chirality’ ^{119,130–135,145}	Valleytronic devices ^{124,125} , photodetectors ¹⁵⁰ , on-chip communications ^{147–149}
Spatial–momentum	Superchiral-enhanced valley polarization ^{35–37} , moiré exciton emission ^{156–161} , combined ‘true’ and ‘false’ chirality ¹⁶²	Chiral light sources ^{35–37} , twistronics ^{156–161} , flexible chirality tuning ¹⁶²

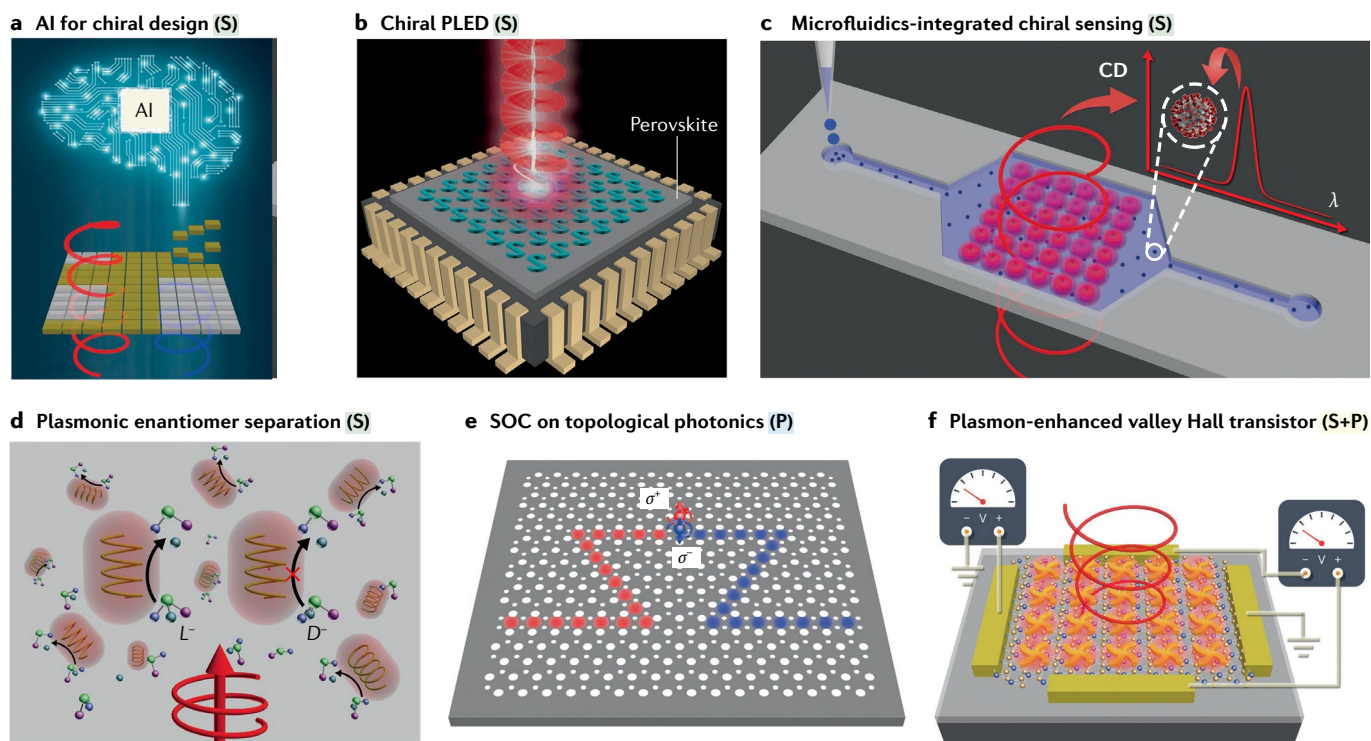


Fig. 5 | Future developments in nanoscopic chiroptics. **a** | Applying artificial intelligence (AI) for the design of chiral nanostructures. **b** | Patterning perovskite materials into chiral geometries for the chiral perovskite light-emitting diode (PLED). **c** | Integrating bound state in the continuum metasurfaces that possess strong superchiral fields onto microfluidics devices for advanced chiral sensing. **d** | Utilizing chiral plasmonic nanostructures for the enhanced enantiomer separation of chiral compounds. **e** | Exploiting the spin–orbital coupling (SOC) phenomenon on topological photonic crystals for non-reciprocal quantum devices. **f** | Integrating chiral plasmonic nanostructures with transition metal dichalcogenide monolayers for the polarization-sensitive, room-temperature valley Hall transistor. CD, circular dichroism; P, momentum; S, spatial.

and mass production of chiral plasmonic nanostructures with large g -factors have made progress in recent years^{76,87}. This is expected to lead to the industrial application of plasmonic enantiomer separation for the production of chiral drugs and vaccines.

In the momentum dimension, the rise of topological photonics, as a new paradigm of nanoscale chiral interfaces¹⁶⁸, provides a SOC platform to control light–matter interactions at the quantum level. Spin-direction locking could be enabled for the coupling of chiral quantum emitters and topological waveguides^{169,170}, and these waveguide modes are robust against tight bends and defects¹⁷¹ (FIG. 5e). As a result, the SOC in topological photonics could empower the development of low-loss and compact non-reciprocal quantum devices, such as optical isolators, circulators and cascaded quantum systems. Another promising trend in nanoscopic chiroptics is to merge different components into an integrated system for achieving a synergistic effect. Valley Hall transistors based on TMDC monolayers have been demonstrated only at cryogenic temperature¹²⁵, and the small volume of light–matter interactions has restricted the

efficiency of the valley Hall effect. These problems can be potentially compensated by the localized enhanced near field of plasmonic nanostructures (FIG. 5f). Moreover, if chiral plasmonic nanostructures are used, the transistor can further acquire the sensitivity to the incident polarization. The chirality-induced spin selectivity effect is another promising direction, giving rise to chiral spintronics^{172–174}. Apart from the above-mentioned applications, we also foresee the potential of nanoscopic chiroptics in reconfigurable chiroptics, data storage and spin-controlled optical devices.

Yang Chen^{1,2}, Wei Du^{3,4}, Qing Zhang¹, Oscar Ávalos-Ovando⁵, Jing Wu⁶, Qing-Hua Xu⁷, Na Liu^{8,9}, Hiromi Okamoto¹⁰, Alexander O. Govorov^{5,11}, Qihua Xiong^{12,13} and Cheng-Wei Qiu¹⁴

¹Department of Electrical and Computer Engineering, National University of Singapore, Singapore, Singapore.

²CAS Key Laboratory of Mechanical Behaviour and Design of Materials, Department of Precision Machinery and Precision Instrumentation, University of Science and Technology of China, Hefei, China.

³Division of Physics and Applied Physics, School of Physical and Mathematical Sciences, Nanyang Technological University, Singapore, Singapore.

⁴Institute of Functional Nano and Soft Materials (FUNSOM), Soochow University, Suzhou, China.

⁵Department of Physics and Astronomy, Ohio University, Athens, OH, USA.

⁶Institute of Materials Research and Engineering (IMRE), Agency for Science, Technology and Research (A*STAR), Singapore, Singapore.

⁷Department of Chemistry, National University of Singapore, Singapore, Singapore.

⁸2nd Physics Institute, University of Stuttgart, Stuttgart, Germany.

⁹Max Planck Institute for Solid State Research, Stuttgart, Germany.

¹⁰Institute for Molecular Science and the Graduate University for Advanced Studies (SOKENDAI), Okazaki, Aichi, Japan.

¹¹Institute of Fundamental and Frontier Sciences, University of Electronic Science and Technology of China, Chengdu, China.

¹²State Key Laboratory of Low-Dimensional Quantum Physics and Department of Physics, Tsinghua University, Beijing, China.

¹³Beijing Academy of Quantum Information Sciences (BAQIS), Beijing, China.

¹⁴e-mail: qihua_xiong@tsinghua.edu.cn; chengwei.qiu@nus.edu.sg

<https://doi.org/10.1038/s42254-021-00391-6>
Published online 15 November 2021

1. Kelvin, W. T. B. *The Molecular Tactics of a Crystal* (Clarendon Press, 1894).
2. McNaught, A. D., Wilkinson, A. *Compendium of Chemical Terminology* Vol. 1669 (Blackwell Science, 1997).
3. Moss, G. P. Basic terminology of stereochemistry (IUPAC Recommendations 1996). *Pure Appl. Chem.* **68**, 2193–2222 (1996).

4. Arago, F. Mémoire sur une modification particulière qu'éprouvent les rayons lumineux dans leur passage à travers certains corps diaphanes et sur plusieurs autres nouveaux phénomènes d'optique. *Moniteur* **73**, 282–284 (1811).
5. Pasteur, L. Sur les relations qui peuvent exister entre la forme cristalline, la composition chimique et le sens de la polarization rotatoire. *Ann. Chim. Phys.* **24**, 442–459 (1848).
6. Barron, L. D. *Molecular Light Scattering and Optical Activity* (Cambridge Univ. Press, 2004).
7. Leung, D., Kang, S. O. & Anslin, E. V. Rapid determination of enantiomeric excess: a focus on optical approaches. *Chem. Soc. Rev.* **41**, 448–479 (2012).
8. Kumar, J. et al. Detection of amyloid fibrils in Parkinson's disease using plasmonic chirality. *Proc. Natl Acad. Sci. USA* **115**, 3225–3230 (2018).
9. Martínez-Girón, A. B., Marina, M. L. & Crego, A. L. Chiral separation of a basic drug with two chiral centers by electrokinetic chromatography for its pharmaceutical development. *J. Chromatogr. A* **1467**, 427–435 (2016).
10. Long, G. et al. Chiral-perovskite optoelectronics. *Nat. Rev. Mater.* **5**, 423–439 (2020).
11. Schaibley, J. R. et al. Valleytronics in 2D materials. *Nat. Rev. Mater.* **1**, 16055 (2016).
12. Moloney, M. P., Govan, J., Loudon, A., Mukhina, M. & Gun'ko, Y. K. Preparation of chiral quantum dots. *Nat. Protoc.* **10**, 558–573 (2015).
13. Papakostas, A. et al. Optical manifestations of planar chirality. *Phys. Rev. Lett.* **90**, 107404 (2003).
14. Gansel, J. K. et al. Gold helix photonic metamaterial as broadband circular polarizer. *Science* **325**, 1513–1515 (2009).
15. Valev, V. K., Baumberg, J. J., Sibilia, C. & Verbiest, T. Chirality and chiroptical effects in plasmonic nanostructures: fundamentals, recent progress, and outlook. *Adv. Mater.* **25**, 2517–2534 (2013).
16. Hentschel, M., Schaferling, M., Duan, X., Giessen, H. & Liu, N. Chiral plasmonics. *Sci. Adv.* **3**, e1602735 (2017).
17. Collins, J. T. et al. Chirality and chiroptical effects in metal nanostructures: fundamentals and current trends. *Adv. Opt. Mater.* **5**, 1700182 (2017).
18. Plum, E., Fedotov, V. A. & Zheludev, N. I. Optical activity in extrinsically chiral metamaterial. *Appl. Phys. Lett.* **93**, 191911 (2008).
19. Zambrana-Puyalto, X., Vidal, X. & Molina-Terriza, G. Angular momentum-induced circular dichroism in non-chiral nanostructures. *Nat. Commun.* **5**, 4922 (2014).
20. Kakkar, T. et al. Superchiral near fields detect virus structure. *Light Sci. Appl.* **9**, 195 (2020).
21. Feis, J. et al. Helicity-preserving optical cavity modes for enhanced sensing of chiral molecules. *Phys. Rev. Lett.* **124**, 035201 (2020).
22. Hu, J., Lawrence, M. & Dionne, J. A. High quality factor dielectric metasurfaces for ultraviolet circular dichroism spectroscopy. *ACS Photonics* **7**, 36–42 (2019).
23. Mohammadi, E. et al. Accessible superchiral near-fields driven by tailored electric and magnetic resonances in all-dielectric nanostructures. *ACS Photonics* **6**, 1939–1946 (2019).
24. Mohammadi, E. et al. Nanophotonic platforms for enhanced chiral sensing. *ACS Photonics* **5**, 2669–2675 (2018).
25. Raziman, T. V., Godiksen, R. H., Müller, M. A. & Curto, A. G. Conditions for enhancing chiral nanophotonics near achiral nanoparticles. *ACS Photonics* **6**, 2583–2589 (2019).
26. Solomon, M. L., Hu, J., Lawrence, M., García-Etxarri, A. & Dionne, J. A. Enantiospecific optical enhancement of chiral sensing and separation with dielectric metasurfaces. *ACS Photonics* **6**, 43–49 (2018).
27. Droulias, S. & Bougas, L. Absolute chiral sensing in dielectric metasurfaces using signal reversals. *Nano Lett.* **20**, 5960–5966 (2020).
28. García-Guirado, J., Svedendahl, M., Puigdollers, J. & Quidant, R. Enhanced chiral sensing with dielectric nanoresonators. *Nano Lett.* **20**, 585–591 (2020).
29. Chen, Y., Zhao, C., Zhang, Y. & Qiu, C.-w. Integrated molar chiral sensing based on high-Q metasurface. *Nano Lett.* **20**, 8696–8703 (2020).
30. Koshelev, K., Jahani, Y., Tittl, A., Altug, H. & Kivshar, Y. *Enhanced Circular Dichroism and Chiral Sensing with Bound States in the Continuum* (Optical Society of America, 2019).
31. Yao, K. & Liu, Y. Enhancing circular dichroism by chiral hotspots in silicon nanocube dimers. *Nanoscale* **10**, 8779–8786 (2018).
32. Khorashad, L. K. et al. Hot electrons generated in chiral plasmonic nanocrystals as a mechanism for surface photochemistry and chiral growth. *J. Am. Chem. Soc.* **142**, 4193–4205 (2020).
33. Morisawa, K., Ishida, T. & Tsumata, T. Photoinduced chirality switching of metal-inorganic plasmonic nanostructures. *ACS Nano* **14**, 3603–3609 (2020).
34. Saito, K. & Tsumata, T. Chiral plasmonic nanostructures fabricated by circularly polarized light. *Nano Lett.* **18**, 3209–3212 (2018).
35. Li, Z. et al. Tailoring MoS₂ valley-polarized photoluminescence with super chiral near-field. *Adv. Mater.* **30**, e1801908 (2018).
36. Wu, Z., Li, J., Zhang, X., Redwing, J. M. & Zheng, Y. Room-temperature active modulation of valley dynamics in a monolayer semiconductor through chiral Purcell effects. *Adv. Mater.* **31**, e1904132 (2019).
37. Wen, T. et al. Steering valley-polarized emission of monolayer MoS₂ sandwiched in plasmonic antennas. *Sci. Adv.* **6**, ea00019 (2020).
38. Bliokh, K. Y., Rodríguez-Fortuño, F. J., Nori, F. & Zayats, A. V. Spin-orbit interactions of light. *Nat. Photonics* **9**, 796–808 (2015).
39. Liu, T. et al. Chiral plasmonic nanocrystals for generation of hot electrons: toward polarization-sensitive photochemistry. *Nano Lett.* **19**, 1395–1407 (2019).
40. Long, G. et al. Spin control in reduced-dimensional chiral perovskites. *Nat. Photonics* **12**, 528–533 (2018).
41. Xu, X., Yao, W., Xiao, D. & Heinz, T. F. Spin and pseudospins in layered transition metal dichalcogenides. *Nat. Phys.* **10**, 343–350 (2014).
42. Tang, Y. & Cohen, A. E. Optical chirality and its interaction with matter. *Phys. Rev. Lett.* **104**, 163901 (2010).
43. Poulikakos, L. V. et al. Optical chirality flux as a useful far-field probe of chiral near fields. *ACS Photonics* **3**, 1619–1625 (2016).
44. Poulikakos, L. V., Thureja, P., Stollmann, A., De Leo, E. & Norris, D. J. Chiral light design and detection inspired by optical antenna theory. *Nano Lett.* **18**, 4633–4640 (2018).
45. Gilroy, C. et al. Roles of superchirality and interference in chiral plasmonic biodection. *J. Phys. Chem. C* **123**, 15195–15203 (2019).
46. Okamoto, H. Local optical activity of nano-to microscale materials and plasmons. *J. Mater. Chem. C* **7**, 14771–14787 (2019).
47. Stockman, M. I. Nanofocusing of optical energy in tapered plasmonic waveguides. *Phys. Rev. Lett.* **93**, 137404 (2004).
48. Li, W. et al. Circularly polarized light detection with hot electrons in chiral plasmonic metamaterials. *Nat. Commun.* **6**, 8379 (2015).
49. Schäferling, M. *Chiral Nanophotonics* (Springer, 2017).
50. Jack, C. et al. Biomacromolecular stereostructure mediates mode hybridization in chiral plasmonic nanostructures. *Nano Lett.* **16**, 5806–5814 (2016).
51. Kelly, C. et al. Controlling metamaterial transparency with superchiral fields. *ACS Photonics* **5**, 535–543 (2017).
52. Zhang, Q. et al. Unraveling the origin of chirality from plasmonic nanoparticle-protein complexes. *Science* **365**, 1475–1478 (2019).
53. Hsu, C. W., Zhen, B., Stone, A. D., Joannopoulos, J. D. & Soljačić, M. Bound states in the continuum. *Nat. Rev. Mater.* **1**, 16048 (2016).
54. Koshelev, K., Lepeshov, S., Liu, M., Bogdanov, A. & Kivshar, Y. Asymmetric metasurfaces with high-Q resonances governed by bound states in the continuum. *Phys. Rev. Lett.* **121**, 193903 (2018).
55. Narushima, T. & Okamoto, H. Strong nanoscale optical activity localized in two-dimensional chiral metal nanostructures. *J. Phys. Chem. C* **117**, 23964–23969 (2013).
56. Valev, V. K. et al. Plasmonic ratchet wheels: switching circular dichroism by arranging chiral nanostructures. *Nano Lett.* **9**, 3945–3948 (2009).
57. Valev, V. K. et al. Nonlinear superchiral meta-surfaces: tuning molar chirality and disentangling non-reciprocity at the nanoscale. *Adv. Mater.* **26**, 4074–4081 (2014).
58. Valev, V. et al. Distributing the optical near-field for efficient field-enhancements in nanostructures. *Adv. Mater.* **24**, OP208–OP215 (2012).
59. Zu, S. et al. Deep-subwavelength resolving and manipulating of hidden chirality in achiral nanostructures. *ACS Nano* **12**, 3908–3916 (2018).
60. Chen, Y., Gao, J. & Yang, X. Direction-controlled bifunctional metasurface polarizers. *Laser Photonics Rev.* **12**, 1800198 (2018).
61. Narushima, T., Hashiyada, S. & Okamoto, H. Nanoscopic study on developing optical activity with increasing chirality for two-dimensional metal nanostructures. *ACS Photonics* **1**, 732–738 (2014).
62. Okamoto, H., Narushima, T., Nishiyama, Y. & Imura, K. Local optical responses of plasmon resonances visualised by near-field optical imaging. *Phys. Chem. Chem. Phys.* **17**, 6192–6206 (2015).
63. Hashiyada, S., Narushima, T. & Okamoto, H. Imaging chirality of optical fields near achiral metal nanostructures excited with linearly polarized light. *ACS Photonics* **5**, 1486–1492 (2018).
64. Rafiei Miandashli, A., Khosravi Khorashad, L., Kordesch, M. E., Govorov, A. O. & Richardson, H. H. Experimental and theoretical observation of photothermal chirality in gold nanoparticle helicoids. *ACS Nano* **14**, 4188–4195 (2020).
65. Spaeth, P. et al. Circular dichroism measurement of single metal nanoparticles using photothermal imaging. *Nano Lett.* **19**, 8934–8940 (2019).
66. Kong, X.-T., Khosravi Khorashad, L., Wang, Z. & Govorov, A. O. Photothermal circular dichroism induced by plasmon resonances in chiral metamaterial absorbers and bolometers. *Nano Lett.* **18**, 2001–2008 (2018).
67. Horrer, A. et al. Local optical chirality induced by near-field mode interference in achiral plasmonic metamolecules. *Nano Lett.* **20**, 509–516 (2020).
68. Wang, M. et al. Reconfigurable plasmonic diastereomers assembled by DNA origami. *ACS Nano* **13**, 13702–13708 (2019).
69. Kuwata-Gonokami, M. et al. Giant optical activity in quasi-two-dimensional planar nanostructures. *Phys. Rev. Lett.* **95**, 227401 (2005).
70. Fedotov, V. A. et al. Asymmetric propagation of electromagnetic waves through a planar chiral structure. *Phys. Rev. Lett.* **97**, 167401 (2006).
71. Faryad, M. & Lakhtakia, A. The circular Bragg phenomenon. *Adv. Opt. Photonics* **6**, 225–292 (2014).
72. Zhang, L., Wang, T., Shen, Z. & Liu, M. Chiral nanoarchitectonics: towards the design, self-assembly, and function of nanoscale chiral twists and helices. *Adv. Mater.* **28**, 1044–1059 (2016).
73. Merg, A. D. et al. Peptide-directed assembly of single-helical gold nanoparticle superstructures exhibiting intense chiroptical activity. *J. Am. Chem. Soc.* **138**, 13655–13663 (2016).
74. Han, B., Zhu, Z., Li, Z., Zhang, W. & Tang, Z. Conformation modulated optical activity enhancement in chiral cysteine and Au nanorod assemblies. *J. Am. Chem. Soc.* **136**, 16104–16107 (2014).
75. Shinmori, H. & Mochizuki, C. Strong chiroptical activity from achiral gold nanorods assembled with proteins. *Chem. Commun.* **53**, 6569–6572 (2017).
76. Lu, J. et al. Enhanced optical asymmetry in supramolecular chiroplasmonic assemblies with long-range order. *Science* **371**, 1368–1374 (2021).
77. Zhou, C., Duan, X. & Liu, N. DNA-nanotechnology-enabled chiral plasmonics: from static to dynamic. *Acc. Chem. Res.* **50**, 2906–2914 (2017).
78. Kuzyk, A. et al. Reconfigurable 3D plasmonic metamolecules. *Nat. Mater.* **13**, 862–866 (2014).
79. Schreiber, R. et al. Chiral plasmonic DNA nanostructures with switchable circular dichroism. *Nat. Commun.* **4**, 2948 (2013).
80. Kuzyk, A. et al. DNA-based self-assembly of chiral plasmonic nanostructures with tailored optical response. *Nature* **483**, 311–314 (2012).
81. Zhang, D. Y. & Seelig, G. Dynamic DNA nanotechnology using strand-displacement reactions. *Nat. Chem.* **3**, 103–113 (2011).
82. Dong, Y., Yang, Z. & Liu, D. DNA nanotechnology based on i-motif structures. *Acc. Chem. Res.* **47**, 1853–1860 (2014).
83. Gerling, T., Wagenbauer, K. F., Neuner, A. M. & Dietz, H. Dynamic DNA devices and assemblies formed by shape-complementary, non-base pairing 3D components. *Science* **347**, 1446–1452 (2015).
84. Kamiya, Y. & Asanuma, H. Light-driven DNA nanomachine with a photoresponsive molecular engine. *Acc. Chem. Res.* **47**, 1663–1672 (2014).
85. Im, S. W. et al. Chiral surface and geometry of metal nanocrystals. *Adv. Mater.* **32**, 1905758 (2020).
86. Lee, H. E. et al. Amino-acid- and peptide-directed synthesis of chiral plasmonic gold nanoparticles. *Nature* **556**, 360–365 (2018).

87. Gonzalez-Rubio, G. et al. Micelle-directed chiral seeded growth on anisotropic gold nanocrystals. *Science* **368**, 1472–1477 (2020).
88. Zheng, G. et al. Tuning the morphology and chiroptical properties of discrete gold nanorods with amino acids. *Angew. Chem. Int. Ed.* **57**, 16452–16457 (2018).
89. Milton, F. P., Govan, J., Mukhina, M. V. & Gun'ko, Y. K. The chiral nano-world: chiroptically active quantum nanostructures. *Nanoscale Horiz.* **1**, 14–26 (2016).
90. Zhang, Y. et al. Tunable chiral metal organic frameworks toward visible light-driven asymmetric catalysis. *Sci. Adv.* **3**, e1701162 (2017).
91. Lu, Y. et al. Homochiral MOF-polymer mixed matrix membranes for efficient separation of chiral molecules. *Angew. Chem. Int. Ed.* **58**, 16928–16935 (2019).
92. Ma, J. et al. Chiral 2D perovskites with a high degree of circularly polarized photoluminescence. *ACS Nano* **13**, 3659–3665 (2019).
93. Chen, C. et al. Circularly polarized light detection using chiral hybrid perovskite. *Nat. Commun.* **10**, 1927 (2019).
94. Ben-Moshe, A., Maoz, B. M., Govorov, A. O. & Markovich, G. Chirality and chiroptical effects in inorganic nanocrystal systems with plasmon and exciton resonances. *Chem. Soc. Rev.* **42**, 7028–7041 (2013).
95. Ben-Moshe, A., Govorov, A. O. & Markovich, G. Enantioselective synthesis of intrinsically chiral mercury sulfide nanocrystals. *Angew. Chem.* **125**, 1313–1317 (2013).
96. Wang, L., Urbas, A. M. & Li, Q. Nature-inspired emerging chiral liquid crystal nanostructures: from molecular self-assembly to DNA mesophase and nanocolloids. *Adv. Mater.* **32**, 1801335 (2020).
97. Saeva, F., Olin, G. & Chu, J. Circular dichroism of trigonal selenium formed in a chiral polymer matrix. *Mol. Cryst. Liq. Cryst.* **41**, 5–9 (1977).
98. Otis, G. et al. Enantioselective crystallization of chiral inorganic crystals of ϵ -Zn(OH)₂ with amino acids. *Angew. Chem. Int. Ed.* **59**, 20924–20929 (2020).
99. Zhang, S. et al. Negative refractive index in chiral metamaterials. *Phys. Rev. Lett.* **102**, 023901 (2009).
100. Gorkunov, M. V., Antonov, A. A. & Kivshar, Y. S. Metasurfaces with maximum chirality empowered by bound states in the continuum. *Phys. Rev. Lett.* **125**, 093903 (2020).
101. Overvig, A., Yu, N. & Alù, A. Chiral quasi-bound states in the continuum. *Phys. Rev. Lett.* **126**, 073001 (2021).
102. Dixon, J., Lawrence, M., Barton, D. R. III & Dionne, J. Self-isolated Raman lasing with a chiral dielectric metasurface. *Phys. Rev. Lett.* **126**, 123201 (2021).
103. Ni, J. et al. Three-dimensional chiral microstructures fabricated by structured optical vortices in isotropic material. *Light Sci. Appl.* **6**, e17011 (2017).
104. Esposito, M. et al. Nanoscale 3D chiral plasmonic helices with circular dichroism at visible frequencies. *ACS Photonics* **2**, 105–114 (2015).
105. Esposito, M. et al. Triple-helical nanowires by tomographic rotatory growth for chiral photonics. *Nat. Commun.* **6**, 6484 (2015).
106. Wang, M. et al. Subwavelength polarization optics via individual and coupled helical traveling-wave nanoantennas. *Light Sci. Appl.* **8**, 76 (2019).
107. Chen, Y., Yang, X. & Gao, J. 3D Janus plasmonic helical nanoapertures for polarization-encrypted data storage. *Light Sci. Appl.* **8**, 45 (2019).
108. Chen, Y., Yang, X. & Gao, J. Spin-controlled wavefront shaping with plasmonic chiral geometric metasurfaces. *Light Sci. Appl.* **7**, 84 (2018).
109. Frese, D., Wei, Q., Wang, Y., Huang, L. & Zentgraf, T. Nonreciprocal asymmetric polarization encryption by layered plasmonic metasurfaces. *Nano Lett.* **19**, 3976–3980 (2019).
110. Cui, Y., Kang, L., Lan, S., Rodrigues, S. & Cai, W. Giant chiral optical response from a twisted-arc metamaterial. *Nano Lett.* **14**, 1021–1025 (2014).
111. Zhao, Y., Belkin, M. A. & Alu, A. Twisted optical metamaterials for planarized ultrathin broadband circular polarizers. *Nat. Commun.* **3**, 870 (2012).
112. Kan, T. et al. Enantiomeric switching of chiral metamaterial for terahertz polarization modulation employing vertically deformable MEMS spirals. *Nat. Commun.* **6**, 8422 (2015).
113. Liu, Z. et al. Nano- kirigami with giant optical chirality. *Sci. Adv.* **4**, eaat4436 (2018).
114. Wang, Q. et al. Reflective chiral meta-holography: multiplexing holograms for circularly polarized waves. *Light Sci. Appl.* **7**, 25 (2018).
115. Kan, Y. et al. Metasurface-enabled generation of circularly polarized single photons. *Adv. Mater.* **32**, 1907832 (2020).
116. Arteaga, O. et al. Relation between 2D/3D chirality and the appearance of chiroptical effects in real nanostructures. *Opt. Express* **24**, 2242–2252 (2016).
117. Khorasaninejad, M., Ambrosio, A., Kanhaiya, P. & Capasso, F. Broadband and chiral binary dielectric meta-holograms. *Sci. Adv.* **2**, e1501258 (2016).
118. Xiao, T. H., Cheng, Z. & Goda, K. Giant optical activity in an all-dielectric spiral nanoflower. *Small* **14**, 1800485 (2018).
119. Zanotto, S. et al. Optomechanics of chiral dielectric metasurfaces. *Adv. Opt. Mater.* **8**, 1901507 (2020).
120. Hu, J. et al. All-dielectric metasurface circular dichroism waveplate. *Sci. Rep.* **7**, 41893 (2017).
121. Jaggard, D., Mickelson, A. & Pappas, C. On electromagnetic waves in chiral media. *Appl. Phys.* **18**, 211–216 (1979).
122. Semmani, B., Flannery, J., Al Maruf, R. & Bajcsy, M. Spin-preserving chiral photonic crystal mirror. *Light Sci. Appl.* **9**, 23 (2020).
123. Soumyanarayanan, A., Reyren, N., Fert, A. & Panagopoulos, C. Emergent phenomena induced by spin-orbit coupling at surfaces and interfaces. *Nature* **539**, 509–517 (2016).
124. Lee, J., Mak, K. F. & Shan, J. Electrical control of the valley Hall effect in bilayer MoS₂ transistors. *Nat. Nanotechnol.* **11**, 421–425 (2016).
125. Mak, K. F., McGill, K. L., Park, J. & McEuen, P. L. The valley Hall effect in MoS₂ transistors. *Science* **344**, 1489–1492 (2014).
126. Wang, G. et al. Colloquium: Excitons in atomically thin transition metal dichalcogenides. *Rev. Mod. Phys.* **90**, 021001 (2018).
127. Cao, T. et al. Valley-selective circular dichroism of monolayer molybdenum disulphide. *Nat. Commun.* **3**, 887 (2012).
128. Zeng, H., Dai, J., Yao, W., Xiao, D. & Cui, X. Valley polarization in MoS₂ monolayers by optical pumping. *Nat. Nanotechnol.* **7**, 490–493 (2012).
129. Mak, K. F., He, K., Shan, J. & Heinz, T. F. Control of valley polarization in monolayer MoS₂ by optical helicity. *Nat. Nanotechnol.* **7**, 494–498 (2012).
130. Ritchie, B. Theory of the angular distribution of photoelectrons ejected from optically active molecules and molecular negative ions. *Phys. Rev. A* **13**, 1411 (1976).
131. Cherepkov, N. Circular dichroism of molecules in the continuous absorption region. *Chem. Phys. Lett.* **87**, 344–348 (1982).
132. Schönhense, G. et al. Circular dichroism in photoemission from surfaces. *Surf. Sci.* **251**, 132–135 (1991).
133. Westphal, C., Bamsmann, J., Getzlaff, M. & Schönhense, G. Circular dichroism in the angular distribution of photoelectrons from oriented CO molecules. *Phys. Rev. Lett.* **63**, 151 (1989).
134. Chandra, N. Circular dichroism in photoionization of oriented nonlinear molecules. *Phys. Rev. A* **39**, 2256 (1989).
135. Verbiest, T., Kauranen, M., Van Rompaey, Y. & Persoons, A. Optical activity of anisotropic achiral surfaces. *Phys. Rev. Lett.* **77**, 1456 (1996).
136. Barron, L. D. True and false chirality and absolute asymmetric synthesis. *J. Am. Chem. Soc.* **108**, 5539–5542 (1986).
137. Barron, L. D. True and false chirality and parity violation. *Chem. Phys. Lett.* **123**, 423–427 (1986).
138. Barron, L. Symmetry and molecular chirality. *Chem. Soc. Rev.* **15**, 189–223 (1986).
139. Barron, L. D. False chirality, absolute enantioselection and CP violation: Pierre Curie's legacy. *Magnetochemistry* **6**, 5 (2020).
140. Plum, E. et al. Metamaterials: optical activity without chirality. *Phys. Rev. Lett.* **102**, 113902 (2009).
141. Plum, E., Fedotov, V. A. & Zheludev, N. I. Specular optical activity of achiral metasurfaces. *Appl. Phys. Lett.* **108**, 141905 (2016).
142. Wang, Y. et al. Giant circular dichroism of large-area extrinsic chiral metal nanorecents. *Sci. Rep.* **8**, 3351 (2018).
143. Mao, L., Liu, K., Zhang, S. & Cao, T. Extrinsic 2D-chiral metamirror in near-infrared region. *ACS Photonics* **7**, 375–383 (2019).
144. Zhu, A. Y. et al. Giant intrinsic chiro-optical activity in planar dielectric nanostructures. *Light Sci. Appl.* **7**, 17158 (2018).
145. Ren, H. & Gu, M. Angular momentum-reversible near-unitary bisignate circular dichroism. *Laser Photonics Rev.* **12**, 1700255 (2018).
146. Lin, J. et al. Polarization-controlled tunable directional coupling of surface plasmon polaritons. *Science* **340**, 331–334 (2013).
147. Pan, D., Wei, H., Gao, L. & Xu, H. Strong spin-orbit interaction of light in plasmonic nanostructures and nanocircuits. *Phys. Rev. Lett.* **117**, 166803 (2016).
148. Lefier, Y., Salut, R., Suarez, M. A. & Grosjean, T. Directing nanoscale optical flows by coupling photon spin to plasmon extrinsic angular momentum. *Nano Lett.* **18**, 38–42 (2018).
149. Thomaschewski, M., Yang, Y., Wolff, C., Roberts, A. S. & Bozhevolnyi, S. I. On-chip detection of optical spin-orbit interactions in plasmonic nanocircuits. *Nano Lett.* **19**, 1166–1171 (2019).
150. Feng, F., Si, G., Min, C., Yuan, X. & Somekh, M. On-chip plasmonic spin-Hall nanograting for simultaneously detecting phase and polarization singularities. *Light Sci. Appl.* **9**, 95 (2020).
151. Junge, C., O'shea, D., Volz, J. & Rauschenbeutel, A. Strong coupling between single atoms and nontransverse photons. *Phys. Rev. Lett.* **110**, 213604 (2013).
152. Luxmoore, I. et al. Interfacing spins in an InGaAs quantum dot to a semiconductor waveguide circuit using emitted photons. *Phys. Rev. Lett.* **110**, 037402 (2013).
153. Petersen, J., Volz, J. & Rauschenbeutel, A. Chiral nanophotonic waveguide interface based on spin-orbit interaction of light. *Science* **346**, 67–71 (2014).
154. Gong, S. H., Alpeggiani, F., Sciacca, B., Garnett, E. C. & Kuipers, L. Nanoscale chiral valley-photon interface through optical spin-orbit coupling. *Science* **359**, 443–447 (2018).
155. Sun, L. et al. Separation of valley excitons in a MoS₂ monolayer using a subwavelength asymmetric groove array. *Nat. Photonics* **13**, 180–184 (2019).
156. Rivera, P. et al. Interlayer valley excitons in heterobilayers of transition metal dichalcogenides. *Nat. Nanotechnol.* **13**, 1004–1015 (2018).
157. Yu, H., Liu, G.-B., Tang, J., Xu, X. & Yao, W. Moiré excitons: From programmable quantum emitter arrays to spin-orbit-coupled artificial lattices. *Sci. Adv.* **3**, e1701696 (2017).
158. Seyler, K. L. et al. Signatures of moiré-trapped valley excitons in MoSe₂/WS₂ heterobilayers. *Nature* **567**, 66–70 (2019).
159. Alexeev, E. M. et al. Resonantly hybridized excitons in moiré superlattices in van der Waals heterostructures. *Nature* **567**, 81–86 (2019).
160. Jin, C. et al. Observation of moiré excitons in WS₂/WS₂ heterostructure superlattices. *Nature* **567**, 76–80 (2019).
161. Tran, K. et al. Evidence for moiré excitons in van der Waals heterostructures. *Nature* **567**, 71–75 (2019).
162. Zanotto, S. et al. Photonic bands, superchirality, and inverse design of a chiral minimal metasurface. *Nanophotonics* **8**, 2291–2301 (2019).
163. Chen, Z. & Segev, M. Highlighting photonics: looking into the next decade. *eLight* **1**, 2 (2021).
164. Ma, W. et al. Deep learning for the design of photonic structures. *Nat. Photonics* **15**, 77–90 (2020).
165. Ma, W., Cheng, F. & Liu, Y. Deep-learning-enabled on-demand design of chiral metamaterials. *ACS Nano* **12**, 6326–6334 (2018).
166. Wetzstein, G. et al. Inference in artificial intelligence with deep optics and photonics. *Nature* **588**, 39–47 (2020).
167. Konishi, K. et al. Circularly polarized light emission from semiconductor planar chiral nanostructures. *Phys. Rev. Lett.* **106**, 057402 (2011).
168. Lodahl, P. et al. Chiral quantum optics. *Nature* **541**, 473–480 (2017).
169. Barik, S. et al. A topological quantum optics interface. *Science* **359**, 666–668 (2018).
170. Mehrabad, M. J. et al. Chiral topological photonics with an embedded quantum emitter. *Optica* **7**, 1690–1696 (2020).
171. Haldane, F. & Raghu, S. Possible realization of directional optical waveguides in photonic crystals with broken time-reversal symmetry. *Phys. Rev. Lett.* **100**, 013904 (2008).
172. Göhler, B. et al. Spin selectivity in electron transmission through self-assembled monolayers of double-stranded DNA. *Science* **331**, 894–897 (2011).
173. Ray, K., Ananthavel, S., Waldeck, D. & Naaman, R. Asymmetric scattering of polarized electrons by organized organic films of chiral molecules. *Science* **283**, 814–816 (1999).
174. Yang, S.-H., Naaman, R., Paltiel, Y. & Parkin, S. S. P. Chiral spintronics. *Nat. Rev. Phys.* **3**, 328–343 (2021).

Acknowledgements

The authors thank N. Zheludev for his valuable suggestions. C.Y. acknowledges the support from the start-up funding of University of Science and Technology of China and the CAS Pioneer Hundred Talents Program. C.-W.Q. acknowledges financial support from the grant No. R-261-518-004-720 from Advanced Research and Technology Innovation Centre (ARTIC). Q.-H.X. and C.-W.Q. acknowledge financial support from Singapore MOR tier 2 Grant (R-143-000-A68-112). W.D. acknowledges financial support from a Singapore National Research Foundation-Agence Nationale de la Recherche (NRF-ANR) grant (no. NRF2017-NRF-ANR005 2DCHIRAL). O.Á.-O. and A.O.G. acknowledge the generous support from the United States-Israel Binational Science Foundation (BSF). N.L. acknowledges financial support from

the European Research Council (ERC Dynamic Nano) grant and from the Max Planck Society (Max Planck Fellow Program). H.O. acknowledges financial support from JSPS Grants-in-Aid for Scientific Research (KAKENHI grant nos. 15H02161 and 16H06505). Q.X. gratefully acknowledges the National Natural Science Foundation of China (no. 12020101003, and no. 92056204), strong support from the State Key Laboratory of Low-Dimensional Quantum Physics and start-up grant from Tsinghua University.

Author contributions

The authors contributed equally to all aspects of the article.

Competing interests

The authors declare no competing interests.

Peer review information

Nature Reviews Physics thanks Zhiyong Tang and the other, anonymous, reviewers for their contribution to the peer review of this work.

Publisher's note

Springer Nature remains neutral with regard to jurisdictional claims in published maps and institutional affiliations.

Supplementary information

The online version contains supplementary material available at <https://doi.org/10.1038/s42254-021-00391-6>.

© Springer Nature Limited 2021, corrected publication 2021